Gravity waves above the Northern Atlantic and Europe during streamer events using Aeolus

Sabine Wüst[1], Lisa Küchelbacher[1], Franziska Trinkl[2], Michael Bittner[1,3]

[1] Erdbeobachtungszentrum, Deutsches Zentrum für Luft- und Raumfahrt Oberpfaffenhofen, 82234 Wessling, Germany
[2] formerly at Erdbeobachtungszentrum, Deutsches Zentrum für Luft- und Raumfahrt Oberpfaffenhofen, 82234 Wessling, Germany, now at Institute of Meteorology and Climate Research - Atmospheric Trace Gases and Remote Sensing, Karlsruhe Institute of Technology, 76131 Karlsruhe, Germany
[3] Institut für Physik, Universität Augsburg, 86159 Augsburg, Germany

Correspondence to: Sabine Wüst (sabine.wuest@dlr.de)

Abstract

Information about the energy density of gravity waves (GWs) is crucial for improving atmosphere models. So far, most space-based studies report on the potential energy, E_{pot}, of GWs, as temperature measurements from satellite are more common. We use Aeolus wind data to derive the kinetic energy density, E_{kin}, of GWs above the Northern Atlantic and Europe. Assuming a perfect instrument performance, this would be a lower limit for the kinetic energy density as Aeolus only measures the horizontal line-of-sight wind. Aeolus, ESA's fourth Earth Explorer Mission, was the first Doppler wind lidar in space and measured vertical profiles of the horizontal line-of-sight wind from the ground to an altitude of ca. 20 – 30 km between 2018 and 2023. With a vertical resolution of 0.25–2 km, Aeolus measurements are in principle well suited for the analysis of GWs. However, the data quality is a challenge for such analyses, as the error of the data is in the range of typical GW amplitudes in the tropo- and stratosphere.

In this study, we derive daily resolved time series of E_{kin} before, during and after two so-called streamer events above the Northern Atlantic and Europe. Streamers are large-scale tongue-like structures of meridionally deflected air masses, which are caused by enhanced planetary wave activity. They are linked to vertical shear of horizontal wind and a pressure system, two possible GW generation mechanisms. We find that there is a temporal coincidence between the enhanced daily averaged E_{kin} and occurrence of the streamer events, which we identified in total column ozone measurements. The derivation of GW signals based on Aeolus data is possible, however, we collected about 100 profiles to statistically reduce the uncertainty of the daily averaged E_{kin}. Compared to non-satellite measurements those daily averaged values are at the upper border.

1 Introduction

Gravity waves (GWs) transport energy and momentum over large distances in the atmosphere without a net mass transport. Primary GW are mostly excited in the lower atmosphere (e.g. Fritts and Alexander, 2003, Pramitha et al. 2015 for a case study). Especially above 75 km height, GWs dominate atmospheric dynamics through the deposition of energy and momentum, even though there exist wave phenomena with larger periods and wavelengths in the atmosphere (Holton, 1982; Houghton, 2002). In the absence of a background wind, energy and momentum are conserved quantities; if the background wind is not zero, the pseudo-energy and -momentum, which can be derived from the energy and some wave parameters, are conserved (Nappo, 2013). Deviations indicate regions in the atmosphere, where GWs irreversibly influence temperature (through (pseudo)energy deposition) and wind (through (pseudo)momentum deposition) while they lead to reversible changes elsewhere. Therefore, two of the main questions when investigating GWs are "how much (pseudo-)energy and (pseudo-)momentum are transported?" and "where are they deposited?". Answers to those questions and a proper parameterization is one key to improving weather and climate models (Eichinger et al. 2020, Alexander et al. 2010).

Information about kinetic and potential energy are often provided as densities in literature (e.g. Ern et al., 2018; Rauthe et al., 2008; Wüst et al., 2016), so energy per unit mass (in $J \cdot kg^{-1}$) or per unit volume (in $J \cdot m^{-3}$). Those quantities are calculated as follows:

$$E_{kin} = \frac{1}{2}(u'^2 + v'^2 + w'^2) \tag{1}$$

where (u', v', w') represent the wind fluctuations due to GWs averaged over one phase, and

$$E_{pot} = \frac{1}{2}\frac{g^2}{N^2}\overline{\left(\frac{T'}{\bar{T}}\right)^2} \tag{2}$$

where g is the acceleration of gravity, N is the Brunt-Väisälä frequency, and T' is the temperature fluctuation, and $\bar{T}$ the background temperature. The overbar denotes the average over one period or multiples of it. The pseudo-energy can be derived by multiplying the sum of the kinetic and potential energy density (per volume) with $\omega/\overline{\hat{\omega}}$ (Nappo, 2013) where $\hat{\omega}$ is the intrinsic frequency ($\hat{\omega} = \omega - u \cdot k - v \cdot l$ with k and l the zonal and meridional wave numbers and u and v the zonal and meridional background wind).

Information about the pseudo-momentum are usually provided in terms of vertical flux of horizontal pseudo-momentum which is

$$(F_{px}, F_{py}) = \bar{\rho}\left(1 - \frac{f^2}{\hat{\omega}^2}\right)(\overline{u'w'}, \overline{v'w'}) \tag{3}$$

F_{px} and F_{py} are the zonal and meridional pseudo-momentum flux components, $\bar{\rho}$ is the atmospheric background density, and f is the Coriolis parameter.

From the equations (1) – (3), it is apparent, that an ideal GW satellite mission would measure both, temperature and wind, in three dimensions. The data would need to be decomposed into background and GW-induced fluctuations. From the fluctuations, the wave vector and the period could be derived. However, for parts of the GW spectrum, equation (3) can be simplified to a version without wind information using linear polarization equations (Ern et al., 2018).

Temperature and wind have been measured from satellite for many years. However, temperature information is available much more frequently than wind measurements. A comprehensive overview about the past satellite-based wind missions in the upper mesosphere and lower thermosphere (UMLT) is given in the introduction of Dhadly et al. (2021). By the end of 2022, three wind missions were in orbit. They all use the principle of Doppler to derive horizontal wind information but they target different species and therefore different altitudes. Two systems are passive and use different airglow emissions and only one is active. The two passive ones were MIGHTI (Michelson Interferometer for Global High-resolution Thermospheric Imaging) on the NASA Ionospheric Connection Explorer (ICON) mission and the TIMED Doppler Interferometer (TIDI, Niciejewski et al., 2006) on the Thermosphere Ionosphere Mesosphere Energetics and Dynamics (TIMED) satellite. MIGHTI delivered vertical profiles of the horizontal wind (height ranges vary, day: 90 – 300 km, night: 90 – 105 km and 200 – 300 km) from 2019 until the end of 2022. It used a Doppler asymmetric spatial heterodyne spectrometer which measures the Doppler shift of the oxygen red and green airglow line at 630.0 and 557.7 nm (Englert et al., 2017). TIDI started its operation more than 20 years ago in 2002. It uses a Fabry Perot interferometer to measure the Doppler shift of individual emission features of the O_2 (0,0) airglow band. From these shifts, horizontal winds between 70 and 120 km during the day and 80 and 105 km at night can be derived (Dhadly et al., 2021). Aeolus (Tan et al., 2008), ESA's fourth Earth Explorer Mission, was an active mission and the first Doppler wind lidar in space. Since 2018, it measured vertical profiles of the horizontal line-of-sight (hlos) wind from ground to the lower stratosphere (20 – 30 km) (Reitebuch et al., 2020; Tan et al., 2008). It carried the Atmospheric LAser Doppler INstrument (ALADIN), which emitted in the UV range (354.8 nm). The Doppler shift of the backscattered radiation (Rayleigh and Mie) was analysed. Aeolus stopped operation on April, 30th 2023 (https://www.eumetsat.int/end-nominal-aeolus-mission-operations, date of access: July, 3rd 2023).

Aeolus wind measurements in principle enable the global derivation of E_{kin}. These data have a vertical resolution of 0.25–2 km, which is well-suited for the analysis of GWs. In the upper troposphere / lower stratosphere (UTLS), GWs typically show amplitudes of 5–10 $m \cdot s^{-1}$ at maximum (e.g., Dutta et al., 2017; Kramer et al., 2015). One challenge is the error (especially the precision, since it still influences the detrended data in contrast to a bias) of Aeolus, which is higher than originally planned for and now in the same order of magnitude as typical GW fluctuations.

This study concentrates on specific dynamical situations called streamers in the upper troposphere / lower stratosphere. Streamers are large-scale tongue-like structures of meridionally deflected air masses (Hocke et al., 2017; Krüger et al., 2005;

Offermann et al., 1999); they are linked to enhanced or breaking planetary waves (PWs). PWs are associated with the formation of pressure systems and influence the position of the tropospheric jet. Enhanced or breaking PWs lead to strong shears of the horizontal wind. Pressure systems, wind shears, but also the jet are possible sources of GWs (e.g., Plougonven and Zhang, 2014; Zülicke and Peters, 2008; Fritts and Nastrom, 1992).

On a case study basis, we investigate whether enhanced daily-averaged E_{kin} can be observed during two pronounced streamer events above the Atlantic in February and November 2020 based on Aeolus measurements. The streamer events were identified in auxiliary data, namely satellite-based total column ozone measurements. Of all the space-based wind sensors listed above, Aeolus is the only one that addresses a prominent region where streamers exist and therefore the region of potential GW generation. The others measure too high up in the atmosphere. Aeolus is therefore the only satellite-based sensor that allows the analysis of E_{kin} in relation to streamers in the height region where GWs are likely to be generated due to that phenomenon. In this case, Aeolus is also superior to ground-based and balloon-based wind measurements, as these are generally not carried out over the Atlantic, one of the regions where streamers preferentially form. As mentioned above, satellite-based vertical temperature profiles are available in the suitable geographical region and height since many years. They allow for the investigation of the potential energy density of gravity waves. However, the ratio of horizontal or vertical kinetic energy density to the potential energy density depends on the vertical orientation of the gravity wave and therefore on its intrinsic frequency, which cannot be deduced or at least only under very specific circumstances from satellite-based data (e.g. by the phase difference method). The use of wind data can therefore not be avoided, when E_{kin} shall be calculated.

The manuscript is structured as follows. The selection and identification of the streamer events which were analysed with respect to GW is given in section 2. Section 3 comprises a description of the data basis, which consist of Aeolus wind data. In section 4, it is explained which Aeolus data we accepted for analysis, how we extracted GW signatures and calculated $E_{kin,}$ as well as its error. In section 5, the temporal evolution of E_{kin} is presented before, during and after two pronounced streamer events. In section 6, the results are discussed. The manuscript ends with a summary and conclusion (section 7).

2 Dynamical situation

As mentioned in the introduction, we focus on streamer events as a generation mechanism for GWs (at their flanks due to strong wind shear but also convective GW since a streamer event is linked to a strong pressure system). When using the term "streamer", one has to provide some further information since this expression is not uniquely defined as pointed out by Krüger et al. (2005) in their introduction. Those authors provide a comprehensive overview about the research on streamers, their effect on mixing, the different definitions, etc. We refer here to large-scale tongue-like structures of meridionally deflected air masses as they are described by Offermann et al. (1999).

Those streamer events can be separated into tropical-subtropical streamers, which transport air from low latitudes into mid latitudes, and polar vortex streamers leading to a mixing of polar air into mid latitudes. Krüger et al. (2005) published a climatology of both streamer types based on 10-year model runs: those events mainly occur during October and May (on the Northern hemisphere) over East Asia and the Atlantic.

Streamers can be traced by ozone, as it has a comparatively long life-time in the lower stratosphere. The reason for streamer events is planetary waves, which are the main drivers of the extratropical circulation. They lead to an irreversible mixing of air masses between the equatorial and polar region (e.g., McIntyre & Palmer 1983, Polvani & Plumb 1992). Normally, streamers can be observed for some days.

Our identification of streamer events is based on global maps of total ozone column measurements (TO3), which are available as a service by DLR (https://atmos.eoc.dlr.de/app/calendar). TO3 is retrieved by the Tropospheric Monitoring Instrument (TROPOMI) on the Sentinel 5 Precursor (S5P) satellite. Whenever no data by TROPOMI/S5P is available, TO3 measurements of the Global Ozone Monitoring Experiment-2 (GOME-2) on the Metop series of satellites are considered. The instruments are nadir-viewing on a near-polar sun-synchronous orbit. TROPOMI/S5P was launched in 2017 and has a spatial resolution of 7 x 7 km^2 with a daily global coverage and a repeat cycle of 17 days (Veefkind et al. 2012). Details on TO3 by TROPOMI/S5P are given by Spurr et al. (2022). The TO3 retrieval is based on the processor of the previous GOME instrument: GOME-2 on Metop-A was launched in 2006 (Metop-B in 2012). It has a spatial resolution of 80 x 40 km^2 and almost a daily global coverage with a repeat cycle of 29 days. See Munro et al. (2006) and Munro et al. (2016) for an overview of the instrument and data processing. Details of the GOME-2 retrieval algorithm can be found in Loyola et al (2011).

In this study, we focus on tropical-subtropical streamers over the Northern Atlantic. The events are identified manually considering the daily TO3 global maps from January 2020 to March 2021. We found three events (approximately 6. – 11. February 2020, 4. – 8. September 2020, and 1. – 8. November 2020) which are, from our perspective, strongest in their evolution, i.e., they have a comparably large spatial size, high intensity (low TO3 concentration), the TO3 low air masses are irreversibly mixed into the surrounding atmosphere (cut-off) and they can clearly be distinguished from other dynamical mixing and vortices.

Figure 1 shows a streamer event over the Northern Atlantic in November 2020. The flanks are comparatively parallel to the longitudes, so it has a strong meridional structure. It reaches latitudes of 70°N. A smaller streamer (which is not considered in this study) can be detected over western North America. There are also ozone-poor air masses above eastern Europe.

Figure 2 shows a streamer event over the Northern Atlantic in February 2020. It is characterized by a diagonal spatial extension from the Sargasso Sea in the south-west reaching the southern parts of Ireland in the north-east at approximately 50°N. Compared to the streamer in November 2020 this one stands out more from its surroundings. This is due to the fact that the ozone content of the surrounding air is higher in February 2020 than in November 2020, while the ozone concentration within the streamer is roughly the same.

The streamer observed in September 2020 is not shown here, as the Aeolus data coverage is not good enough for further analysis (see also section 3).

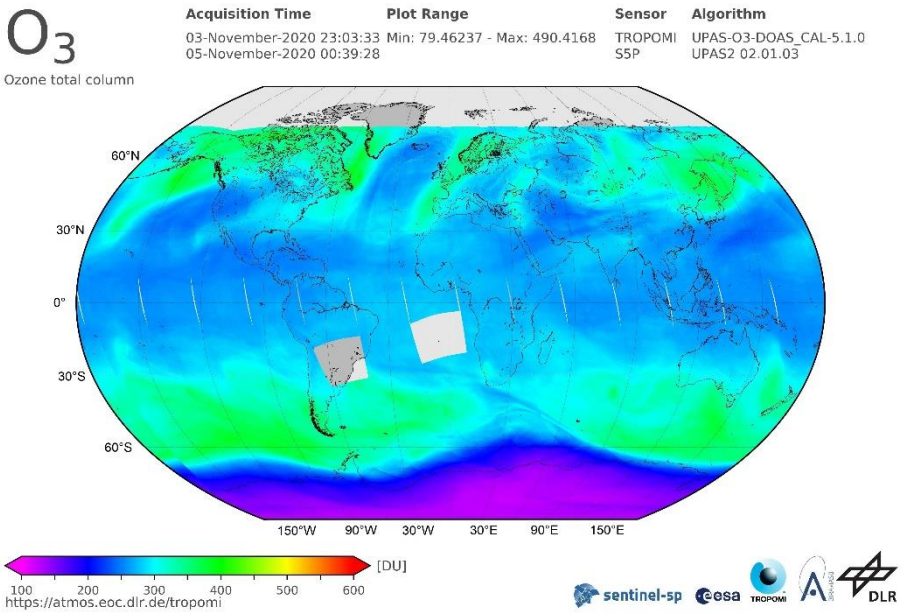

Figure 1 The TO3 measurements taken by TROPOMI/S5P on Nov., 4th 2020 indicate a large streamer event. The starting date cannot be clearly specified due to data gaps. On Nov. 1st a slight signature was already visible above the eastern coast of North America. The streamer moved east ward with time. It was most pronounced above the Northern Atlantic on Nov., 4th. On Nov. 8th, it was not visible any more. Source: These data/products were generated under the auspices of the AC SAF project of the EUMETSAT. The image is provided by DLR (https://atmos.eoc.dlr.de/app/calendar, last access: 28th May 2024) under CC-BY 3.0, the authors made slight changes (moved the colour bar downward, enlarged the latitude and longitude labels).

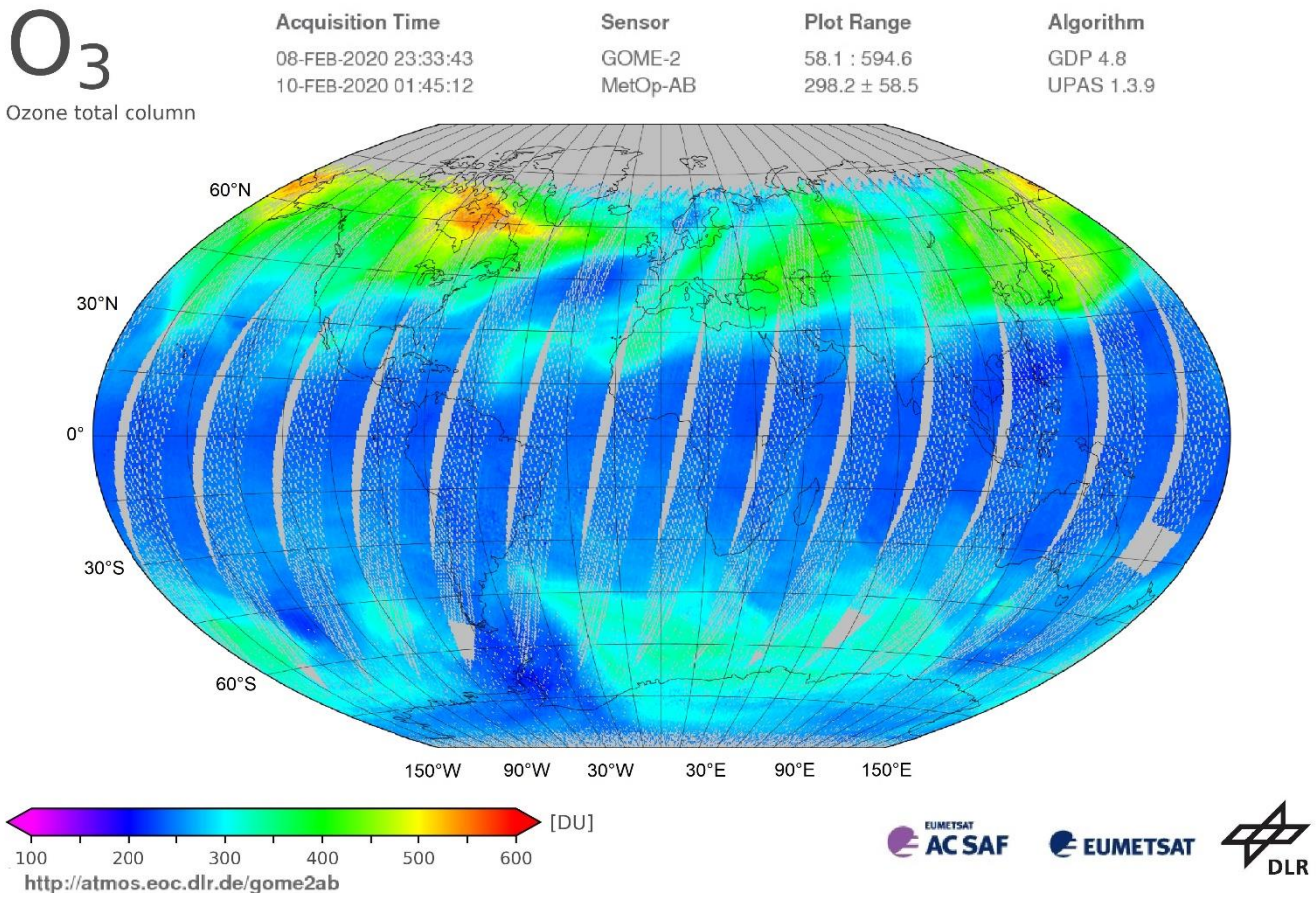

Figure 2 The TO3 measurements taken by GOME-2/MetOp-AB on Feb., 9th 2020 indicate a large streamer event. It started to evolve on Feb., 6th in front of the Eastern coast of Northern America and moved eastward with time. It was most pronounced above the Northern Atlantic on Feb., 9th. On Feb. 12th, it was not visible any more. Data source: These data/products were generated under the auspices of the AC SAF project of the EUMETSAT, image processing was done by the authors analogously to Figure 1.

3 Data basis

Detailed information about the Aeolus instrument is given on the ESA homepage https://www.esa.int/Applications/Observing_the_Earth/FutureEO/Aeolus/Documents_publications (last access: 16th September 2022). Here, only the very basics are summarized. Aeolus was launched on August, 22nd 2018. It carried a Doppler wind lidar (ALADIN, Atmospheric LAser Doppler INstrument), which emitted in the UV range (354.8 nm). The backscattered radiation was collected by a telescope, its Doppler shift was derived and analysed. Aeolus measured both, the Rayleigh and Mie backscattering. The first one originates from molecules, the second one from particles.

Aeolus data are provided as dbl (Data BLock) files from ESA. They contain amongst others vertical profiles of the hlos (horizontal line of sight) wind velocity. We downloaded the level 2B (L2B) data and added a variable which contains the hlos wind corrected for the satellite observation geometry (more information below). We selected the variables which we needed for our analyses with the CODA software in python. Finally, we converted everything to netCDF files. The list of the variables in the netCDF files is given in Table 1.

In the following, we explain how we do the correction of the wind for the satellite geometry. Firstly, a correction of the sign of the wind measurements is necessary, since the hlos wind is given relative to the satellite. Therefore, distinguishing between ascending and descending mode is necessary for providing the hlos wind independent of the satellite observation geometry. Information about the horizontal orientation of the satellite relative to the target in degrees is provided by the variable 'los_azimuth': the target is in the centre of the coordinate system and the azimuth is the angle between the vector pointing from the target to the North and the vector pointing from the target to the satellite. If this angle is larger than 180°, the satellite is west of the target. Since the instrument looks to the right side of the satellite with respect to the flight direction, the satellite is in this case in its ascending orbit branch and vice versa. Hlos has a positive sign, if the wind blows away from the instrument and vice versa. A positive hlos wind is a wind to the East in the ascending branch and to the West in the descending branch. So, in order to become independent of the satellite observation geometry and follow the conventions of atmospheric physics (a wind to the East has a positive sign and vice versa), the sign of the hlos wind must be changed, if the azimuth angle is smaller than 180°.

Hlos wind is available as four observational products: Rayleigh clear, Rayleigh cloudy, Mie clear, and Mie cloudy. For the Rayleigh wind measurements, which represent the majority of the wind measurements, 30 individual measurements are averaged; therefore, each hlos wind value is the horizontal average over 86.4 km (Martin et al., 2021).

Table 1 Overview table of auxiliary data files of Aeolus data.

Variable Names	Variable Description	Variable Units
alt	Height of the wind measurement	m
hlos	Hlos wind	$cm \cdot s^{-1}$

hlos_corrected	Corrected hlos wind dependent on ascending or descending mode	$cm \cdot s^{-1}$
hlos_error	Error estimate reported by the Rayleigh processing algorithm (defined in the Aeolus Level-2B Algorithm Theoretical Baseline Document)	$cm \cdot s^{-1}$
lat	Latitude of the wind measurement	Degrees
lon	Longitude of the wind measurement	Degrees
los_azi	Azimuth of the target-to-satellite pointing vector measured clockwise from north.	degrees
observation_type	Information if the profile is cloudy or clear sky. Values range from 0 to 2 which mean 0 for initialization purposes only 1 cloudy 2 clear	
start_of_obs_datetime	Date and time of first measurement used for wind result	seconds since 2020-10-08 09:09:47.026030976
validity_flag	Indicates if data is valid (1) or invalid (0)	

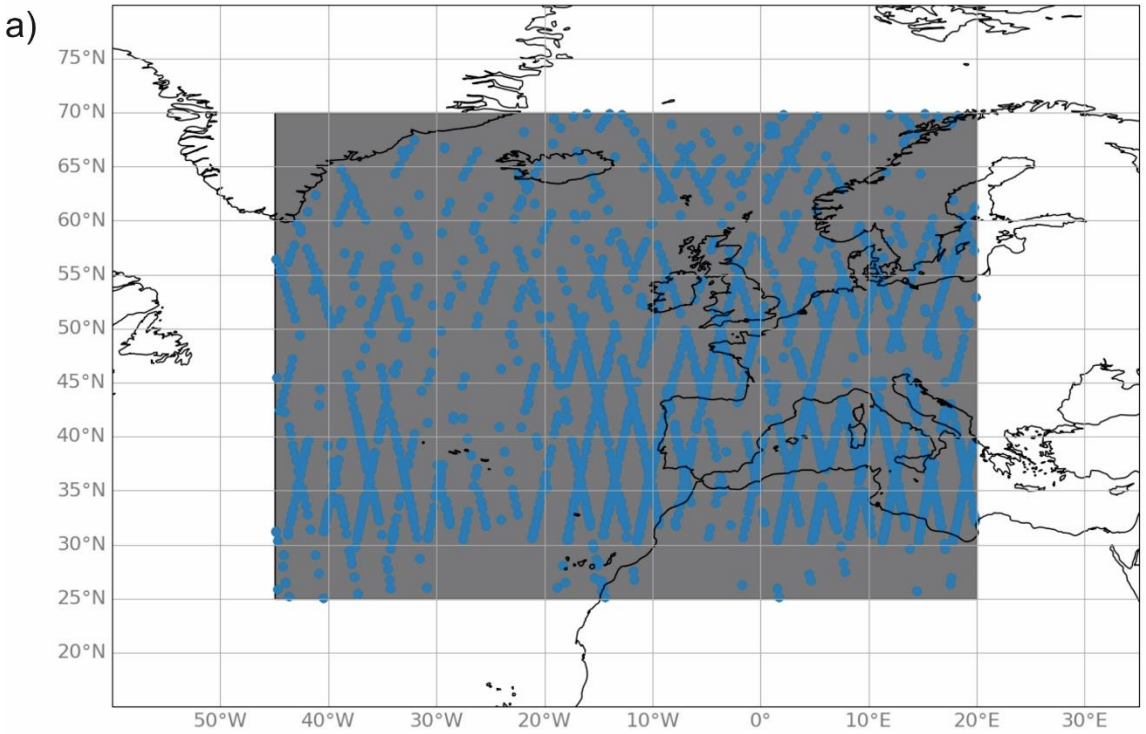
a)
75°N
70°N
65°N
60°N
55°N
50°N
45°N
40°N
35°N
30°N
25°N
20°N
50°W
40°W
30°W
20°W
10°W
0°
10°E
20°E
30°E

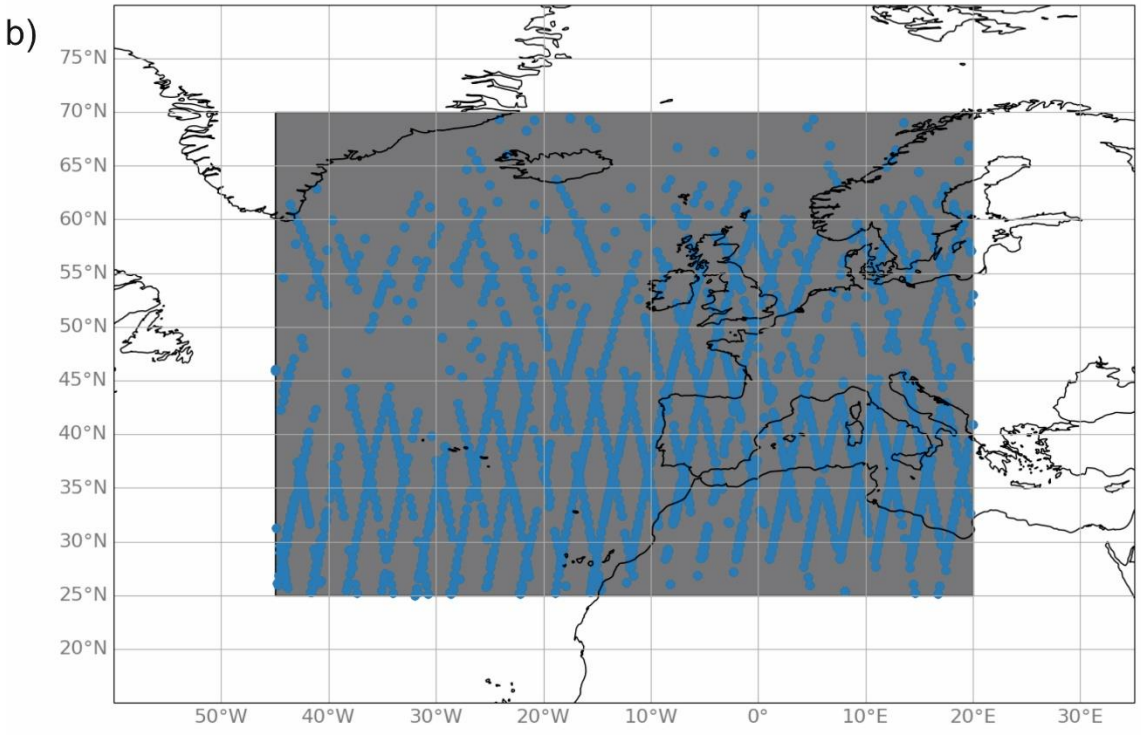
b)
75°N
70°N
65°N
60°N
55°N
50°N
45°N
40°N
35°N
30°N
25°N
20°N
50°W
40°W
30°W
20°W
10°W
0°
10°E
20°E
30°E

Figure 3 Maps showing the region investigated for GW and geographical position of the vertical wind profiles of Aeolus used for the investigation of streamer 1 that was observed in this region from November 3 to November 7, 2020 (a) and streamer 2 observed from February 8 to February 11, 2020 (b). The blue dots refer to the position of all profiles used for generating the time series shown in Figure 8 and Figure 9.

For our analyses, we used only Rayleigh clear wind measurements, which were marked as valid (variable 'validity_flag' equal to 1). Rayleigh clear and Mie cloudy winds have the best quality of the four different wind products. Even though Mie cloudy winds have smaller random errors than Rayleigh clear winds (Rennie et al. 2021), they are rare above the upper troposphere. Especially the stratosphere is very suitable for gravity waves analysis as it is stably stratified. Therefore, Rayleigh clear winds are preferable to Mie cloudy winds for gravity wave analysis. According to the geographical position of the streamer events, which was discussed in the previous section, the spatial focus for the investigation of GW in this manuscript is on 25–70°N and 45°W–20°E (see Figure 3). For Aeolus, different processor baselines are available, which cover different observation periods. In this study, we used data referring to the year 2020, this is baseline 11 (2B11). A consistent reprocessed data set covering the Aeolus whole observation time was not available for the time of our calculations.

For our purpose, only the statistical error of the hlos wind (the precision) is of importance as long as the systematic one (the bias) stays approximately constant with height, as we will explain later. Unfortunately, ESA does not provide individual information about the magnitude of the different error types, only an integrated value (hlos_error, see Table 1) is given. Martin et al. (2021) separated this error into a systematic and a statistical one. In their study, the authors used Rayleigh winds with an estimated error of 6 $m \cdot s^{-1}$ at maximum; they refer to 2B02–2B07 (September 2018 until December 2019), so to earlier baselines than we do. The absolute bias averaged over the analysed time period is ca. 2 $m \cdot s^{-1}$, but it depends on the data set used for validation and on the ascending or descending orbit (see table 1 of Martin et al. (2021)). To some extent, this is due to the six different processor baselines. Furthermore, there were several updates of the calibration files. The estimated Aeolus instrumental error is given by 4.0 – 4.4 $m \cdot s^{-1}$ for Rayleigh winds (see table 2 of Martin et al. (2021)). It shows a temporal variation, which mainly depends on the laser output energy. Ratynski et al. (2023) compared Aeolus to radiosonde and ground-based lidar data during a longer time period (September 2018 – January 2022, which means 2B02 to 2B13) than Martin et al. (2021) but only at two stations. Furthermore, they did not apply any hlos error threshold. Those authors report an averaged systematic error of -0.92 $m \cdot s^{-1}$ and -0.79 $m \cdot s^{-1}$ and a mean random error of 6.49 $m \cdot s^{-1}$ and 5.37 $m \cdot s^{-1}$ for lidar and radiosondes, respectively. They state that the bias correction of the Aeolus data which took place around mid-April 2020 did not affect the random error. The random error depends on different factors, and the shot-noise from the detection process of the signal photons is the dominating one (Rennie et al., 2021). The stronger the signal, the smaller the random error. The atmospheric signal depends on the output laser pulse energy and the optical efficiency of the transmit-and-receive path, the distance between the satellite and the target, and finally on the amount of signal accumulation (Rennie et al., 2021). The first factor (output laser pulse energy and the optical efficiency of the transmit-and-receive path) varied during the mission, but as we are focussing

here on relatively short time intervals, we assume that the influence is approximately constant. The second factor shows a geographical dependence. The atmospheric signal is indirectly proportional to the distance between the satellite and the target and the distance has a minimum at the Equator but a maximum at the two poles. As our region of investigation is relatively large ranging from 25°N to 70°N, there will be some influence. The amount of signal accumulation depends on the horizontal accumulation length and on the vertical thickness of the bins. The thickness of the bins varies over the profile. It has a minimum at ca. 10 km and at the lower limit of the vertical profile (investigated for November 2020, 25°–70°N, 0°–20°E, calculated was the difference of the mean bin heights for the bin 1 – 21). Nevertheless, one cannot say that the error shows a linear dependence on the thickness, in our case it shows a height dependence being high at the lower part of the profile up to ca. 6 km and approximately constant above. Further information about the Aeolus data, changes to this processing and error can be found in Rennie and Isaksen (2024).

Aeolus 2B data are delivered on 24 height bins. Data at high altitude levels are not available for each Aeolus profile, data at low altitudes suffer from slightly larger errors than other heights (investigated for November 2020, 25°–70°N, 0°–20°E). The histogram of the error of all height bins shows a structure with three maxima (see Figure 4). From this plot, one can conclude that accepting an error larger than ca. 4.5 $m \cdot s^{-1}$ will not enlarge the data basis significantly. In order to find a compromise between profiles which are as long but also as accurate as possible, we decided for two quality criteria: the profiles must cover all height bins 1–21 (with height level 1 the highest altitude) and the error has to be better than 4.5 $m \cdot s^{-1}$ at each height bin.

As mentioned above, there exist three pronounced streamer events during January 2020 to March 2021. In this study, the events in February and November 2020 are analysed. For the streamer in September 2020, there is not enough Aeolus data available to meet our quality criteria.

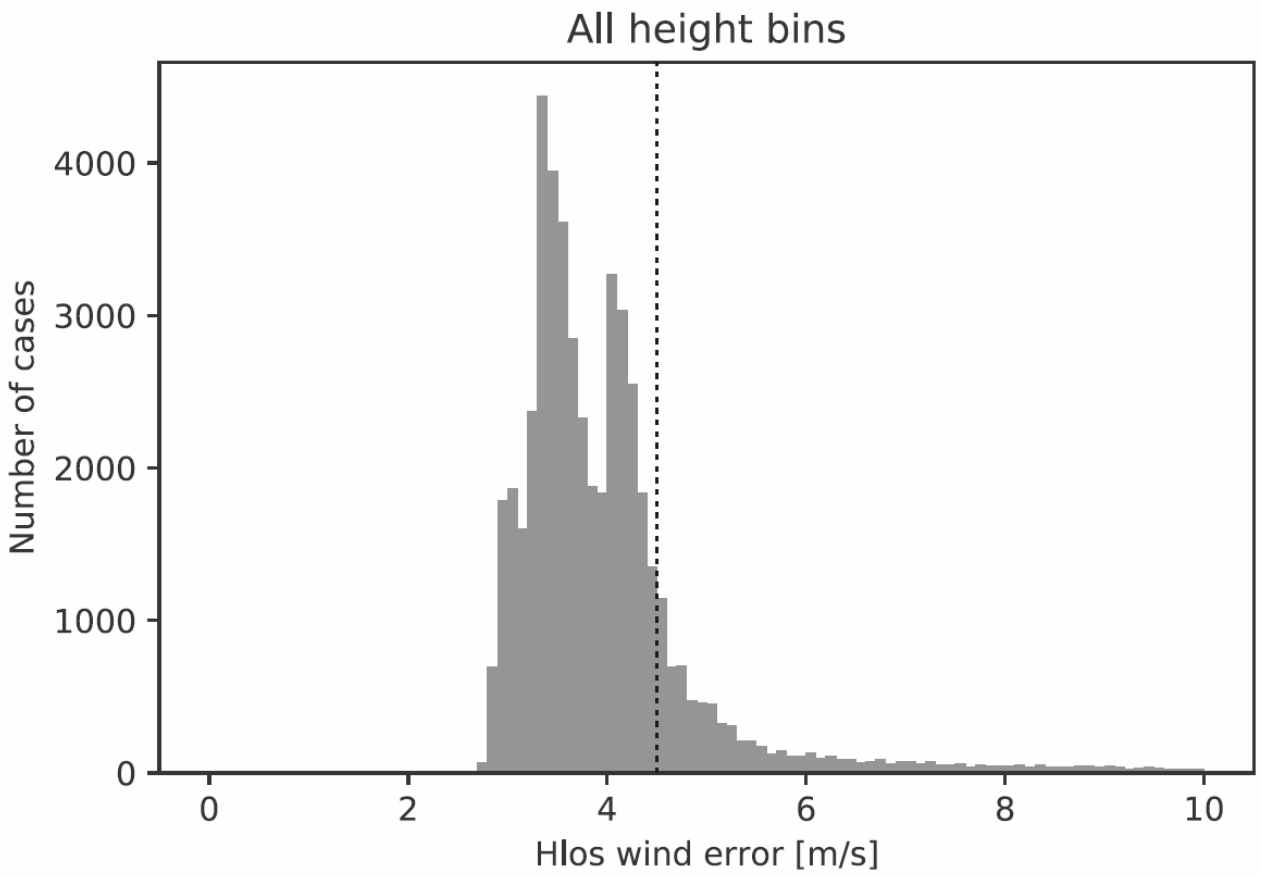

Figure 4 The histogram for the whole November 2020 shows a characteristic structure with three maxima at ca. 2.9 m·s^{-1}, 3.3 m·s^{-1} and 4.1 m·s^{-1}. None of the profiles in the investigated geographical area (25°–70°N, 0°–20°E) has a lower error than ca. 2.7 m·s^{-1}. These values refer to all height bins, so 1 – 24. The vertical dashed line marks an error of 4.5 m·s^{-1}.

4 Analysis

We rely here on cubic splines for the approximation of the atmospheric background, so on piecewise third-order polynomials which are stitched together at the spline sampling points following some mathematical specifications. A cubic spline is adapted individually to each vertical wind profile and subtracted from it. The residuals are analysed further.

The distance of the spline sampling points determines the sensitivity of the spline: according to the Nyquist sampling theorem, a signal with a vertical wavelength of x km, must be sampled at least every 0.5·x km in order to resolve it. Transferred to the spline, this means that a spline sampling point must be set every 0.5·x km. An alternative formulation is: a spline with sampling points every 0.5·x km is sensitive to wavelengths of x km and longer. The residuals include only signals with a vertical wavelength of x km at maximum.

There exist two main challenges for splines. The first one, which is common to all adaptation techniques, is the insufficient approximation of extrema in the background, e.g., the wind maximum in the tropopause. In this case, the spline is too smooth and its subtraction from the original data leads to an artificial signature in the residuals. Secondly, a spline can generate artificial oscillations (at the beginning and the end of a vertical profile or also over the whole height range, if the vertical wavelength to which the spline is sensitive is approximately equal to the vertical wavelength of the GW which is present in the data, see Wüst et al. (2017)). These undesired effects are less pronounced when using the repeating spline approach, i.e., the profile is adapted by splines with the same distance between their sampling points but with varying starting points. Their mean is used as final approximation. This approach is introduced and discussed especially for the derivation of GW signals in Wüst et al. (2017). It is applied here.

The profiles chosen for the GW analysis due to our quality criteria have a length of approximately 16 km and a vertical resolution of ca. 0.8–1.0 km. Therefore, the minimal vertical wavelength to which the spline is sensitive and therefore the maximal vertical wavelength of the residuals can range between ca. 2 km (Nyquist criterion) and 16 km. Since GW with a short vertical wavelength also have small amplitudes in most cases and since the error of Aeolus is relatively large for the investigation of GW in the troposphere, the choice of 2 km as maximal wavelength in the residuals will probably not deliver useful results. The same holds for the other extremum: the choice of a maximal wavelength of 16 km will lead to a coarse approximation of the tropopause wind extremum and therefore to relatively strong artificial signatures in the residuals at the tropopause height. That is why we decide for three different and more moderate maximal vertical wavelengths (5 km, 7.5 km and 10 km). The splines are adapted and the residuals are calculated. For the calculation of the density of kinetic energy E_{kin} knowledge about the three-dimensional wind variations is necessary (see equation (1)).

As mentioned above, Aeolus measures the line-of-sight wind. Due to the orientation of the instrument and the satellite orbit this is to a large extent the zonal wind (this does not hold for polar latitudes, see Krisch et al. (2022)). Using L2B data, one can strictly speaking only calculate a lower bound for E_{kin}. E_{kin} is derived for every height bin. Since the profiles cover

different height ranges, E_{kin} is summed up and divided by the number of values. We call the result mean E_{kin}. It has the unit $\frac{J}{kg}$. The algorithm is sketched in Figure 5. Based on this algorithm, maxima of mean E_{kin} over the area or time period defined at the beginning of the algorithm can be identified, thus GW hotspots in place or time.

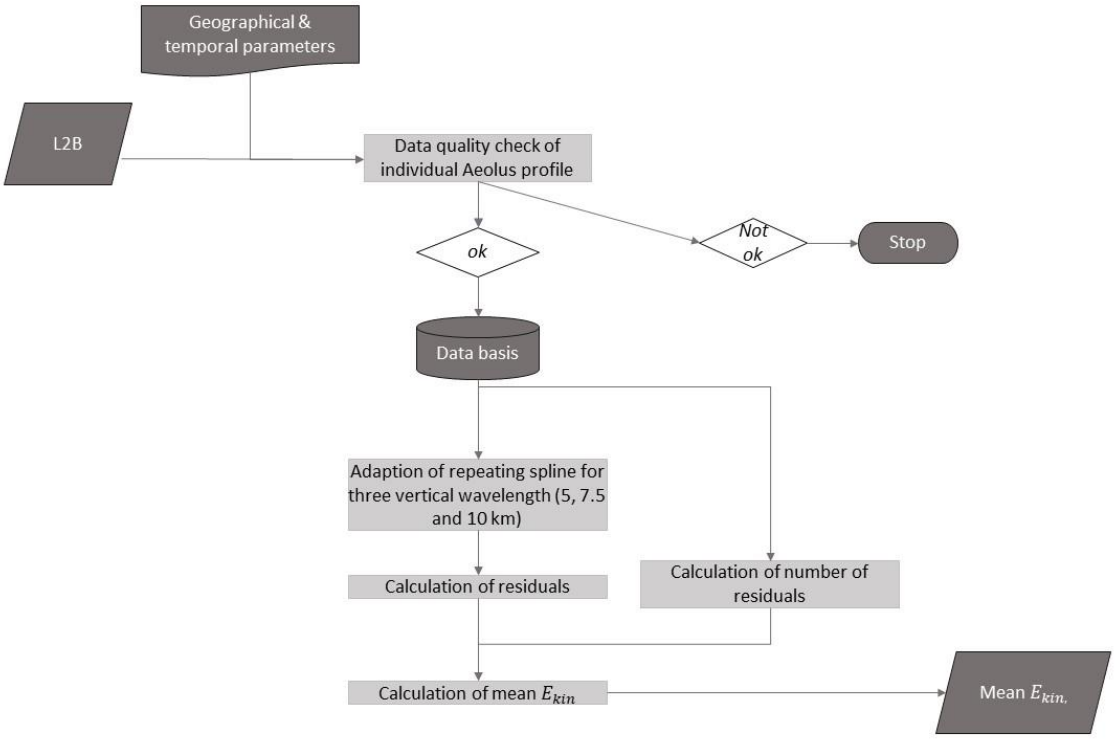

Figure 5 Scheme of the algorithm for the derivation of the mean E_{kin} from Aeolus L2B wind measurements.

An important point in this context is the estimation of the error of E_{kin}. This can be done in a similar way as already demonstrated by Kramer et al. (2016) in their appendix A who used a (non-repeating) cubic spline in order to derive GW signatures from radiosonde-based measurements in the lower stratosphere. Those authors generated a data basis with simulated GW signatures (five different starting amplitudes (0.5 K, 1.0 K, …, 2.5 K), five different values used to increase the amplitudes linear with height (0.05, 0.01, …, 0.25) from 0 – 29.7 km height, 13 different wavelengths (1.0 km, 1.5 km, …, 7 km) and eight different phases (π/8, π/7, …, π)). They arbitrarily constructed five GW, superimposed them on a realistic atmospheric background and detrended the generated profiles with a spline sensitive to wavelengths of 7 km and longer. So, in principle

this spline should be able to remove all GW signatures from the background. They repeated this approach about 1000 times, calculated the difference between the original background and the retrieved one and derived the mean over these differences depending on height in order to estimate the error induced by the spline.

We do some adaptations for our error calculation; the algorithm is sketched in Figure 6. Since the vertical resolution of Aeolus data is coarser compared to radiosondes and therefore less GWs are visible in Aeolus profiles, we superimpose only three oscillations with maximal wavelengths between 2.0 km and 10 km. The height range we investigate covers 1–17 km, the vertical resolution is 800 m. We assume, that the amplitudes (here in $m \cdot s^{-1}$ instead of K as in Kramer et al. (2016)) can grow linearly between 0.05 and 1.95 over the height range. As shown later in section 5 (see Figure 7), this is a valid assumption overall. As background data, we use CIRA (COSPAR International Reference Atmosphere). Since the vertical resolution of CIRA is different to the vertical resolution of Aeolus, a spline is used to adapt the resolution of CIRA to the one of Aeolus. Since we are not only interested in the error due to the spline approximation, but would also like to include the error of Aeolus, we add a value for the measurement uncertainty to the background and the superimposed GW signatures. We accept a maximal error of 4.5 $m \cdot s^{-1}$. As mentioned above, Martin et al. (2021) showed for Aeolus data with an error of 6 $m \cdot s^{-1}$ and better that ca. 2/3 of the error is due to random processes and ca. 1/3 can be attributed to a bias. A systematic bias approximately constant with height is not important for the GW derivation since it will be taken out through the detrending procedure. We check the distribution of the Aeolus error with height for November 2020. Although it shows some height-dependent variation (in general lower in the lower part and higher in the upper), it cannot be modelled by a simple function such as a linear one. Therefore, we calculate the mean value over the used height bins (1–21), which is ca. 3.7 $m \cdot s^{-1}$, and its standard deviation (ca. 0.3 $m \cdot s^{-1}$). Since we already use Aeolus data of relatively high quality, we make the conservative assumption that 1 $m \cdot s^{-1}$ of the 3.7 $m \cdot s^{-1}$ is caused by systematic effects and derive normally distributed values based on a mean of 2.7 $m \cdot s^{-1}$ and the standard deviation mentioned above. For each height, the algorithm arbitrarily chooses the precision from the normally distributed values and the sign.

Then, we detrend the profile with the repeating spline approach which is sensitive to 10 km at minimum and calculate the residuals, which we compare to the original GW signatures. We repeat this process 100 times for different latitudes (40° N, 50° N, and 60° N) and use these values in order to calculate an error for E_{kin}.

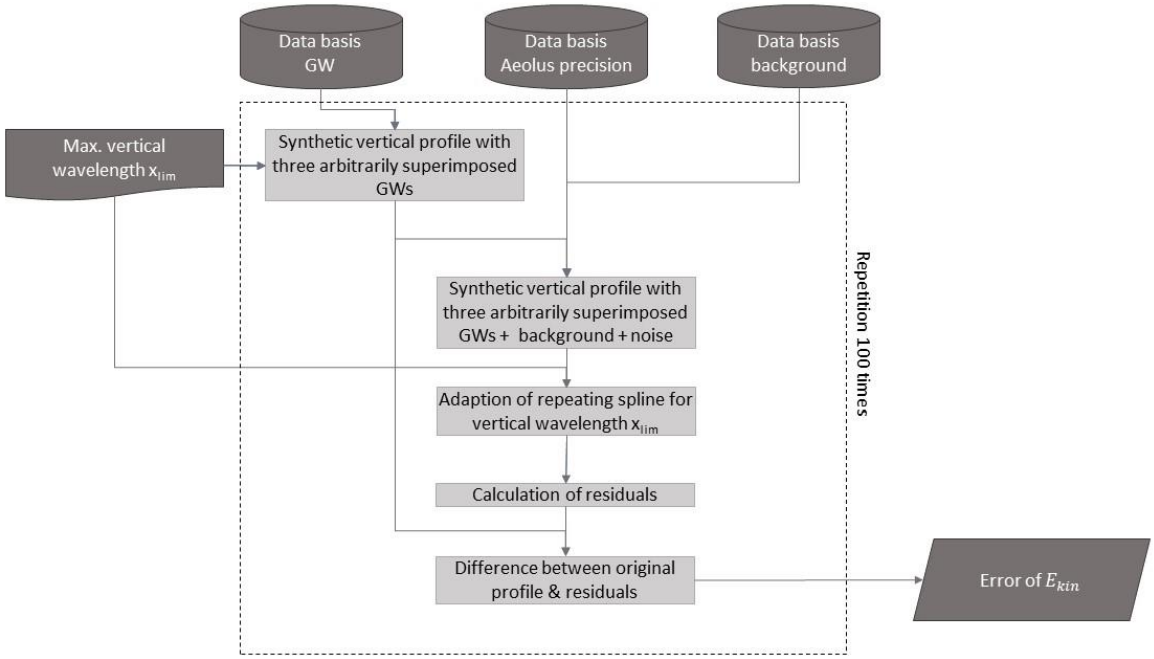

Figure 6 Scheme of the algorithm for the error estimation of E_{kin} from Aeolus L2B wind measurements.

5 Results

We start with the event in November 2020, which shows a more meridional structure than the streamer in February 2020 (see section 2). The November streamer is referred to as streamer 1 in the following. Accordingly, the February streamer is denoted as streamer 2.

Figure 7a shows the vertical profile of the absolute residuals averaged over time for different maximal vertical wavelengths (2750 profiles, from 15th October to 29th November 2020, so including the time of occurrence of streamer 1 as well as approximately the two to three weeks before and after the event). The values of up to 5 $m \cdot s^{-1}$ are in the same order of magnitude as values reported in literature (e.g., by Kramer et al. (2015) or Nath et al. (2009)). Both, negative and positive residuals versus height (Figure 7b) are highly symmetrical: this suggests that, at least on average, the detrending does not introduce strong biases.

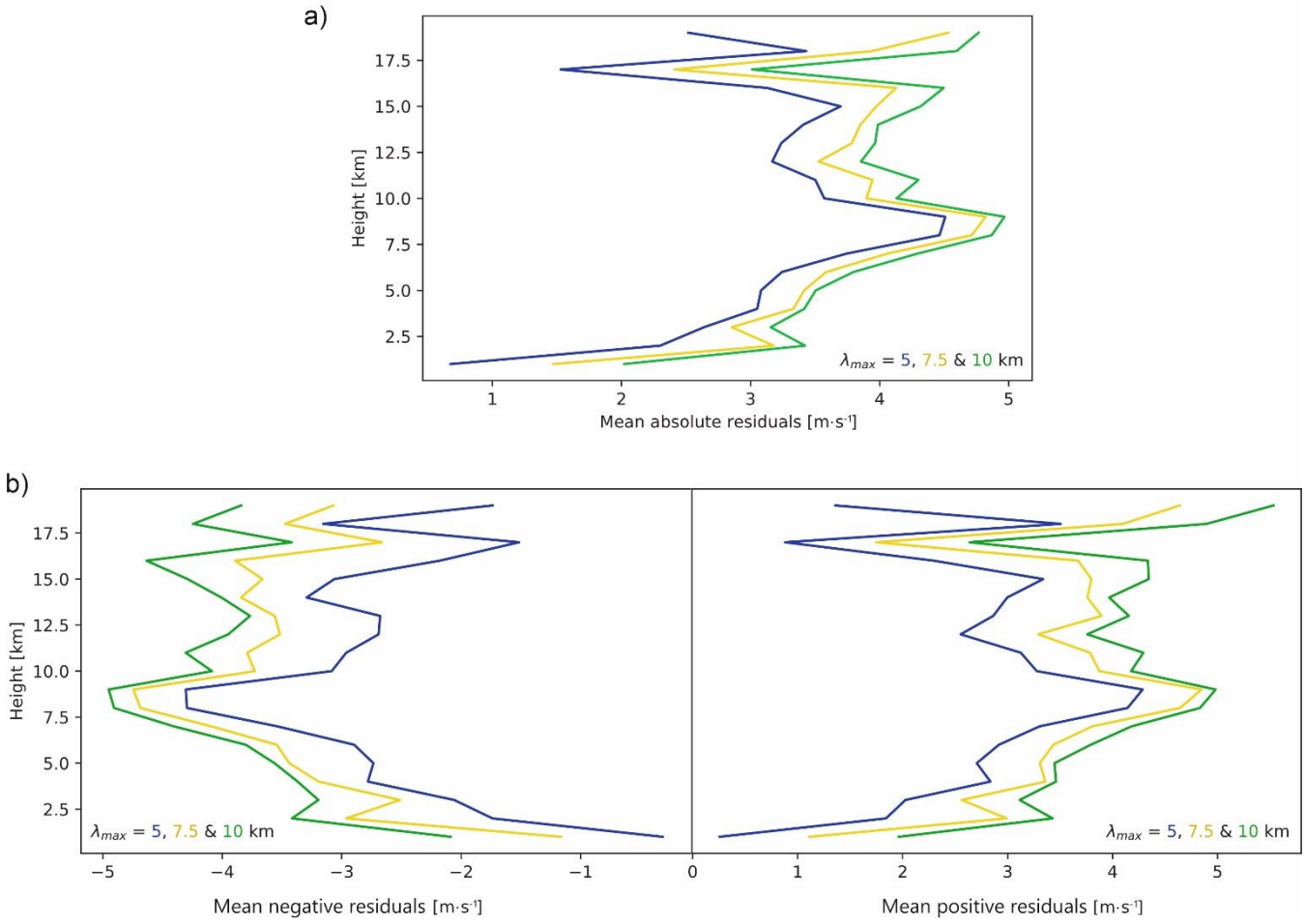

Figure 7 Shown are the absolute residuals per height (a) averaged over 15th October – 29th November 2020 (2750 profiles). The colours refer to the different maximal vertical wavelengths (blue: 5 km, yellow: 7.5 km, and green: 10 km). The profiles originate from the geographical area shown in Figure 3 (25–70°N / 45°W–20°E). Part b) splits the residuals into positive and negative ones.

However, two limitations can be seen in Figure 7:

The first one is that the Aeolus error, which ranges between 2.8 $m \cdot s^{-1}$ and 4.5 $m \cdot s^{-1}$, covers the range of mean residuals. This makes individual Aeolus profiles challenging to use for GW analysis. So either, only very pronounced events are investigated based on Aeolus data such as Banyard et al. (2021) showed it for wind perturbations larger than 10 $m \cdot s^{-1}$, or a larger amount of profiles is collected and the mean residuals are analysed. In the latter case, instead of the individual error, the mean error of the averaged residuals can be used, which is a factor $1/\sqrt{n}$ smaller than the individual error. We rely on the latter solution here.

The second limitation is that there exists a maximum in the vertical profile of the mean absolute residuals between 7.5 km and 10 km height. Even though the repeating spline performs better than the non-repeating one, it cannot be excluded that we see an artificial signature, which should not be interpreted as GW signatures. To exclude this effect of the wind maximum, the residuals are only analysed below 7 km (tropospheric part) and above 11 km (stratospheric part) in the following.

For Figure 7, we calculated the temporal average and showed vertically resolved data. Now in Figure 8, we do it the other way around: we focus on vertically averaged data (split into tropospheric and stratospheric part as mentioned above) and show a time series with daily resolution.

Both, the tropospheric and the stratospheric parts (Figure 8a and b), are not characterized by a single pronounced maximum during mid-October to late November 2020, but there are a number of local maxima. Within the stratosphere or troposphere, the curves for the different wavelengths agree quite well. The agreement is slightly worse, if, for example, the mean E_{kin} of GW with 10 km maximal vertical wavelength of the stratosphere (Figure 8a, green curve) is compared with the corresponding tropospheric curve (Figure 8b, green curve).

The mean E_{kin} in the stratosphere shows a local maximum during 3rd to 5th November for all vertical wavelengths, while this is not the case for the troposphere. The stratospheric maximum is less pronounced for a maximal vertical wavelength of 5 km. Part c) of Figure 8 depicts only the maximum vertical wavelength of 10 km, this time shown with error bars. It is clear that the maximum during November 3rd to 5th is significant.

The values of the error bars come from the algorithm sketched in Figure 6. The error analysis described there was done for different latitudes since the background wind (from CIRA) varies to some extent depending on latitude. For E_{kin} derived from an individual profile, an error of 1.9 – 2.4 $J \cdot kg^{-1}$ or 2.2 $J \cdot kg^{-1}$ on average can be expected (see Table 2). We use this mean value of 2.2 $J \cdot kg^{-1}$ for the calculation of the error bars. Since our analysis relies on ca. 100 profiles per day, the mean error is approximately $\frac{2.2}{\sqrt{100}}\ J \cdot kg^{-1}$.

For streamer 2, the development of the mean E_{kin} is calculated from 1st to 28th February 2020 for a maximal vertical wavelength of 10 km and separated into the tropo- and the stratospheric part (Figure 9). Also in this case, both, the tropospheric and the stratospheric E_{kin}, are not characterized by a single maximum during the occurrence of the streamer but by a number of local maxima. The stratosphere shows a pronounced and significant maximum on February 10th. For the E_{kin} of the troposphere, this is not the case; here E_{kin} is high from February 10th to 14th.

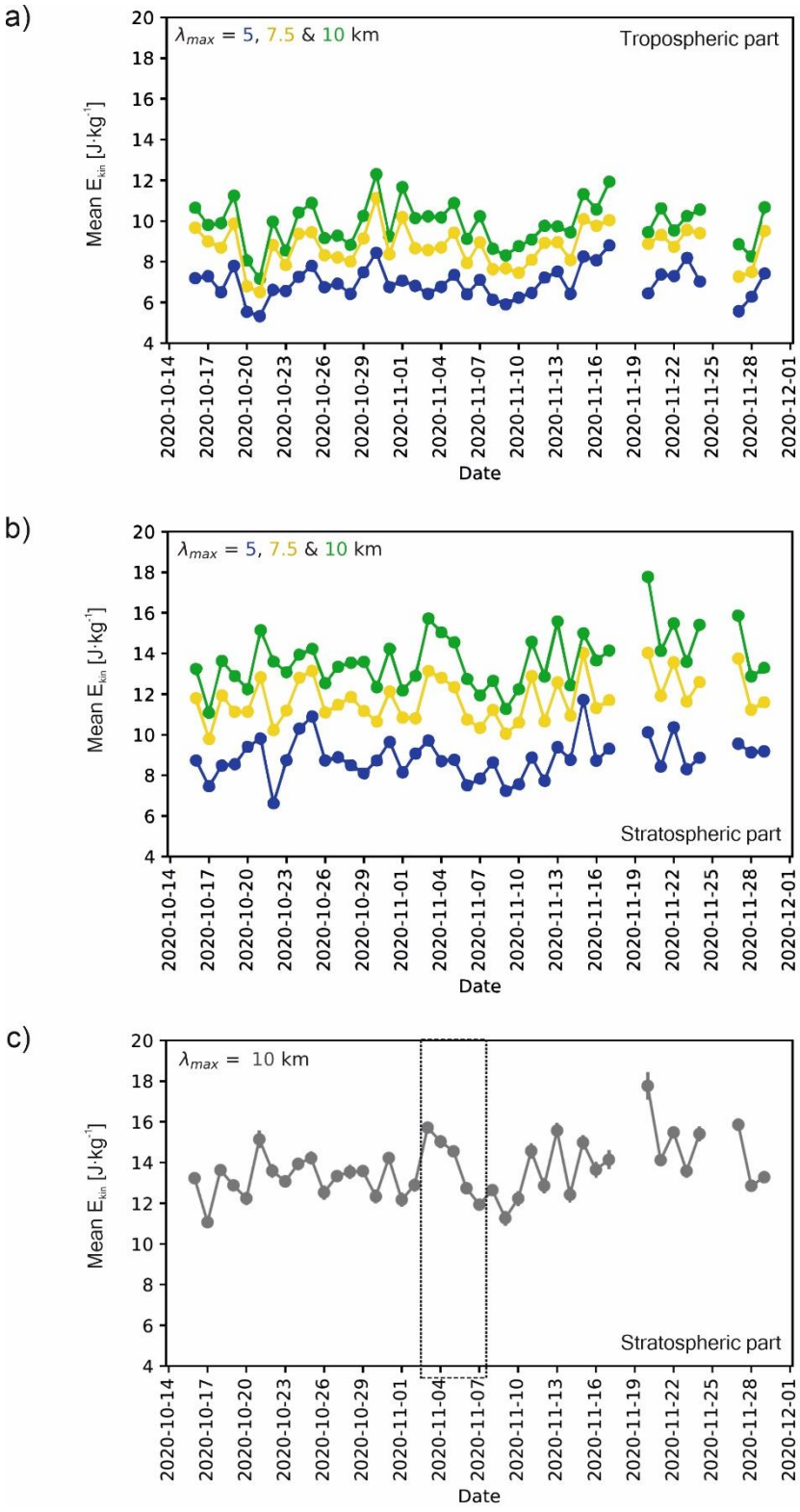
a)
λ_{max} = 5, 7.5 & 10 km
Tropospheric part
Mean E_{kin} [J·kg^{-1}]
Date
b)
λ_{max} = 5, 7.5 & 10 km
Stratospheric part
Mean E_{kin} [J·kg^{-1}]
Date
c)
λ_{max} = 10 km
Stratospheric part
Mean E_{kin} [J·kg^{-1}]
Date

Figure 8 Shown is development of the mean E_{kin} over time. While subplot a) refers to the tropospheric part, the lower two figures depict the stratospheric part. The colour code is the same as in Figure 7 (blue: 5 km, yellow: 7.5 km, and green: 10 km maximal vertical wavelength). Part c) shows only the time series for the maximal vertical wavelength of 10 km. Additionally, error bars are included and the time period 3rd – 7th November 2020, where the streamer could be observed in TO3 measurements above the investigated region, is marked by the dotted lines.

Table 2 Provided is the error of E_{kin} for one individual profile based on 100 arbitrarily generated and detrended vertical GW profiles. The latitudinal dependence is in the range of 11%.

Latitude	Mean error of E_{kin} [J·kg^{-1}]
40°N	2.4
50°N	1.9
60°N	2.2

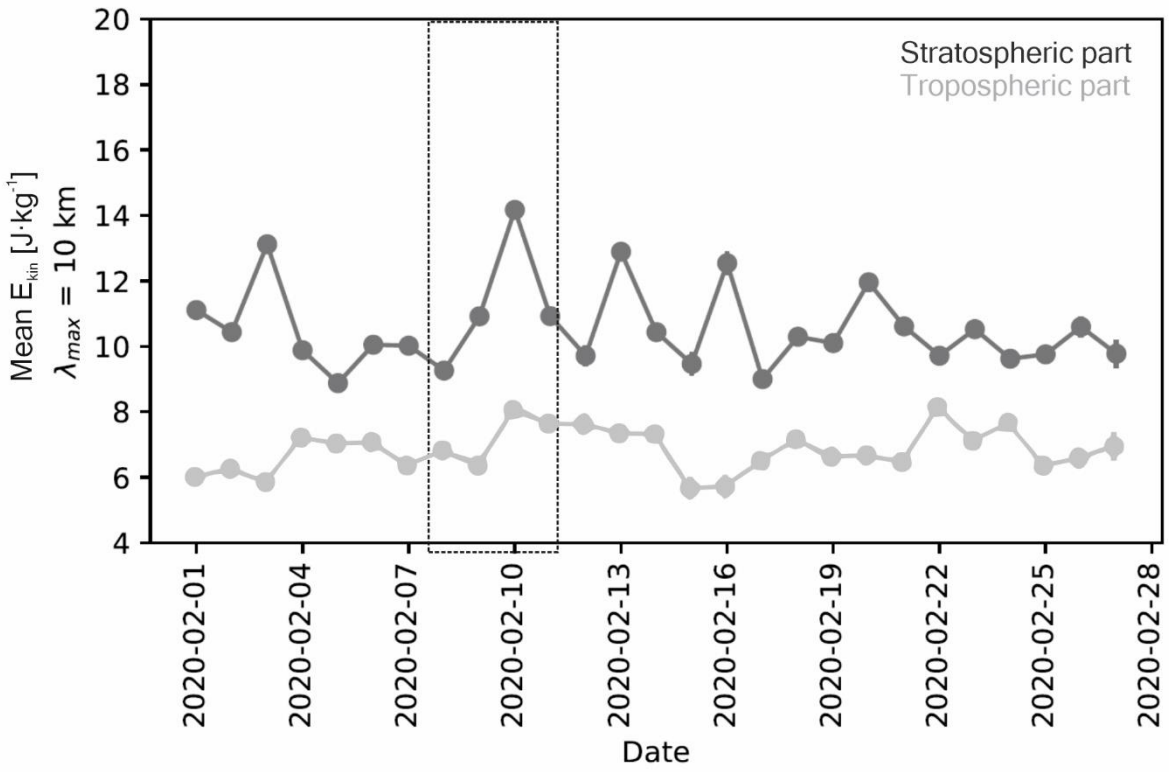

Figure 9 Shown is development of the mean E_{kin} over time for the troposphere and the stratosphere. The dashed rectangle shows the time period of streamer 2 in the investigated geographical region.

6 Discussion

GWs can be generated by a number of processes, where air experiences a vertical momentum (which can be up- or downward). Additionally, GWs can originate due to unstable shears or geostrophic adjustment (accompanying frontal evolution, for example), or they can be the result of an interaction between other GWs (Fritts and Alexander, 2003). Several of those processes occur simultaneously with a streamer such as vertical movements, wind shear, and fronts. GFS data (Global Forecast System) at 250 hPa, for example, show a strong anticyclone, which is linked to downward vertical movement in the centre near the position of the streamer in both cases investigated here (e.g. https://earth.nullschool.net/#2020/11/04/0600Z/wind/isobaric/250hPa/orthographic=-29.56,45.15,312 for streamer 1, and https://earth.nullschool.net/#2020/02/09/0600Z/wind/isobaric/250hPa/orthographic=-29.56,45.15,312 for streamer 2, last access: 27th May 2024). Additionally, a strong vertical shear of the horizontal wind can be observed when addressing different heights. Also frontal activity is present (https://www.wetterzentrale.de/reanalysis.php?jaar=2020&maand=11&dag=4&uur=000&var=45&map=1&model=dwd for streamer 1, and https://www.wetterzentrale.de/reanalysis.php?jaar=2020&maand=2&dag=9&uur=000&var=45&map=1&model=dwd for streamer 2, last access: 27th May 2024). As shown in the section above, we focus on data of the lower stratosphere, which is a stably stratified part of the atmosphere. Besides the vertical momentum on an air parcel, a stable stratification of the surrounding atmosphere is the second prerequisite for the existence of GWs. So, in principle, it is not surprising to observe enhanced GW activity in the stratosphere during a streamer event. However, to our knowledge, such a study has not been published so far.

Additionally, we use Aeolus wind data here. As already mentioned before, the data quality of Aeolus is a challenge for the analysis of GWs as long as they are not very pronounced. While there exist publications, for example, on the validation of Aeolus data (e.g., Khaykin et al. (2020), Ratynski et al. (2023), Witschas et al. (2022)), to our knowledge only one article has been published, which focuses on the analysis of GW from Aeolus data: Banyard et al. (2021) presented a case study for GWs above the tip of South America using amongst others Aeolus data. There, the authors can take advantage of a very pronounced GW event with an amplitude in the range of 10 $m \cdot s^{-1}$, which is approximately twice as large as the averaged amplitude of the waves analysed in this case study (compare e.g. Figure 7). As the error of the Aeolus data is in the range of these averaged amplitudes, the Aeolus data are not per se suitable for individual GW case studies. Focusing on pronounced events as Banyard et al. (2021) did or handling this challenge statistically by covering a large area (see Figure 3) and collecting around 100 profiles per day as we do are two possibilities to make use of Aeolus data for GW analyses.

As already briefly mentioned at the beginning of section 5, the mean residuals of the Aeolus measurements (see Figure 7) are in the same order of magnitude as those reported for other measurements in the literature (e.g., Figure 5 of Kramer et al. (2015), Figure 4 and 6 of Nath et al. (2009), or Figure 5 of Moffat-Griffin et al. (2017)). However, it must be mentioned here

that those literature values are mostly residuals of individual measurements or amplitudes of GWs from radiosonde-based measurements and not averaged residuals. So, there might be a difference in the range of a small factor larger than 1. In comparison with literature values for the density of kinetic energy, the values derived here appear somewhat high (compare Figure 9 of Murphy et al. (2014) who mainly focus on vertical wavelengths of 2 – 3 km and shorter, for example or Figure 7 and 8 of Moffat-Griffin et al. (2017) who focus on vertical wavelengths of 13 km and shorter). Despite the same order of magnitude of the residuals this is possible because quadratic residuals are used to calculate the kinetic energy density. Thus, small differences will be amplified non-linearly. They could be the results of the relatively high Aeolus error, specifically if the error is due to a low precision. However, there are some radiosonde stations that show the same order of magnitude for the density of kinetic energy (10^1 J·kg^{-1}) in their averaged values (see figure 4 and 5 of Yoshiki and Sato (2000)). Nevertheless, a conclusive comparison is difficult here. Firstly, the comparative measurements (radiosondes) are based on a different technique, i.e. they may address different volumes of air than Aeolus (miss-integration error). In addition, there is the movement of the measuring devices during the measurement and the different retrieval of the data. This can lead to a different sensitivity with regard to GWs. Aeolus measures a horizontal line-of-sight velocity; this means that it is particularly sensitive to GWs whose air parcels oscillate horizontally (inertia and mid-frequency GW) and parallel to the line of sight. Finally, the measurements were taken at different times and in different locations.

We find that E_{kin} shows local maxima while a streamer event was present in the investigated geographical region. Nevertheless, E_{kin} is not enhanced during the entire time (8. – 11. February 2020 and 3. – 7. November 2020). This can be due to the position of the specific wave sources or to the direction of wave propagation, which can be oblique, for example. To investigate whether an enhanced spatial resolution, at the cost of temporal resolution, could restrict the potential sources, we gridded the region with a resolution of 7.5° in latitude and 10° in longitude. This corresponds to roughly 800 km in each direction for the mid-point of the addressed geographical region. If a temporal resolution of one week is chosen, the values per pixel range between 2 and 76 (14 – 24 values on average per pixel varying with the calendar week (CW)). Lower values would not be reasonable. The amount of Aeolus data of sufficient quality (as defined above) is not enough, to provide maps which are free of gaps. Decreasing the spatial resolution to improve the pixel covering, is not useful for the purpose of identifying possible wave sources. Therefore, this approach is not further followed here.

Comparing Figure 8c) and Figure 9b) it is noticeable that the structure of Figure 9b) looks more regularly: maxima (of different height) can be observed every 3 – 4 days. In Figure 8c), the time interval between two succeeding maxima varies, one dominating oscillation cannot be identified. As mentioned earlier, streamers are due to enhanced planetary waves and streamers are not the only GW source. The dominance of the 3 – 4 days signature in the time series of E_{kin} during February 2020 suggests the conclusion that maxima of E_{kin} are due to pronounced travelling planetary waves with a period of 3 – 4 days and that other GW sources are less important during that time period. According to Forbes et al. (1995), 3 – 4 days are typical for a travelling

planetary wave with zonal wave number 2. So, Figure 9b) might show a regular effect of a planetary wave 2 on the generation of GW and the identified streamer event in February 2020 might be due to the most pronounced activity of this planetary wave. Here, it should also be stressed that only a part of the GW spectrum can be observed by Aeolus, as is the case for all instruments (e.g., Preusse et al. 2002; Wüst et al., 2006). Aeolus as an off-nadir viewer (35° incidence angle) looks obliquely through the atmosphere and collects all information along the line of sight. GWs with phase fronts not oriented parallel to the line of sight are displayed attenuated in the Aeolus data. Along the track, Aeolus averages approximately over 86 km (see section 3), i.e., only GWs with (in our case) meridional wavelengths larger than 172 km can be detected in Aeolus data (Nyquist criterion). In conclusion, that underpins that E_{kin} is strictly speaking only a lower limit: this is due to the effects just mentioned and to the fact that the instrument measures only along the line of sight and therefore not the whole 3D wind vector. However, a low precision of the Aeolus measurements can lead to a significant high-bias in the derived E_{kin} values.

Finally, we come back to Figure 7 which depicts the averaged absolute residuals over height. When extracting GWs from vertical profiles (this includes not only wind, but also other parameters such as temperature or ozone), it is unfortunately a common problem: not every signal in the residuals can necessarily be attributed to a GW. For individual profiles, this can be solved at least in parts by checking the respective residual profiles for non-GW signals, so for signals that do not match the observed vertical wavelength. For a large number of profiles, some thousands as is the case here, this is only possible in parts. In order to reduce the risk of signals in the residuals that are not attributable to GWs, it is helpful to exclude typical height regions that lead to the generation of "artificial" signals in the residuals. The most important areas here are the atmospheric pauses, in our case the tropopause. That is why we restricted the analysis to the height range below 7 km and above 11 km. Additionally, we used a method (repeating spline) that can better reproduce strong deflections than the classic spline method due to the variation of its starting points. However, we can neither exclude the possibility that we generate no "artificial" signals, nor can we be sure that the maximum in the residuals at about 9 km altitude (Figure 7), which roughly corresponds to the height of the wind maximum, is an artefact. It could also have a physical explanation. GWs generated at lower altitudes increase in amplitude as they propagate to higher altitudes. A horizontal wind that also increases with height will filter the upward propagating GWs. Compared with lower altitudes, the greatest proportion of the upward propagating GWs will be filtered out at the height of the wind maximum. This means that it is possible that an increase in the average GW amplitude will be followed by a minimum. The same applies to the average residuals as extracted from Aeolus. At higher altitudes, the decrease in air density can lead to an increase in the average GW amplitudes and therefore in the Aeolus residuals. Another possibility to explain the increase in the averaged GW amplitudes could be the generation of secondary GWs, the generation of GWs due to strong wind shear at the height of the wind maximum.

Figure 10a) depicts the height of the primary wind maximum of each vertical wind profile used for the derivation of $\boldsymbol{E_{kin}}$, part b) also includes the height of the secondary maximum. Both plots show lower numbers below 7 km height and strongly enhanced values above. Critical layer filtering will therefore mainly affect the height range above 7 km, below 7 km GW can grow in amplitude. The latter can be observed in Figure 7. The global maximum of the Aeolus wind profiles can indeed be

found mainly at 8 – 9 km height, but also to a substantial part at higher altitudes. Arguing that the wind maximum is on average at 8 – 9 km and that this leads to the maximum of the residuals at this height due to possible insufficient detrending, might therefore be too conservative. Including also the second highest maximum does not change the overall view tremendously.

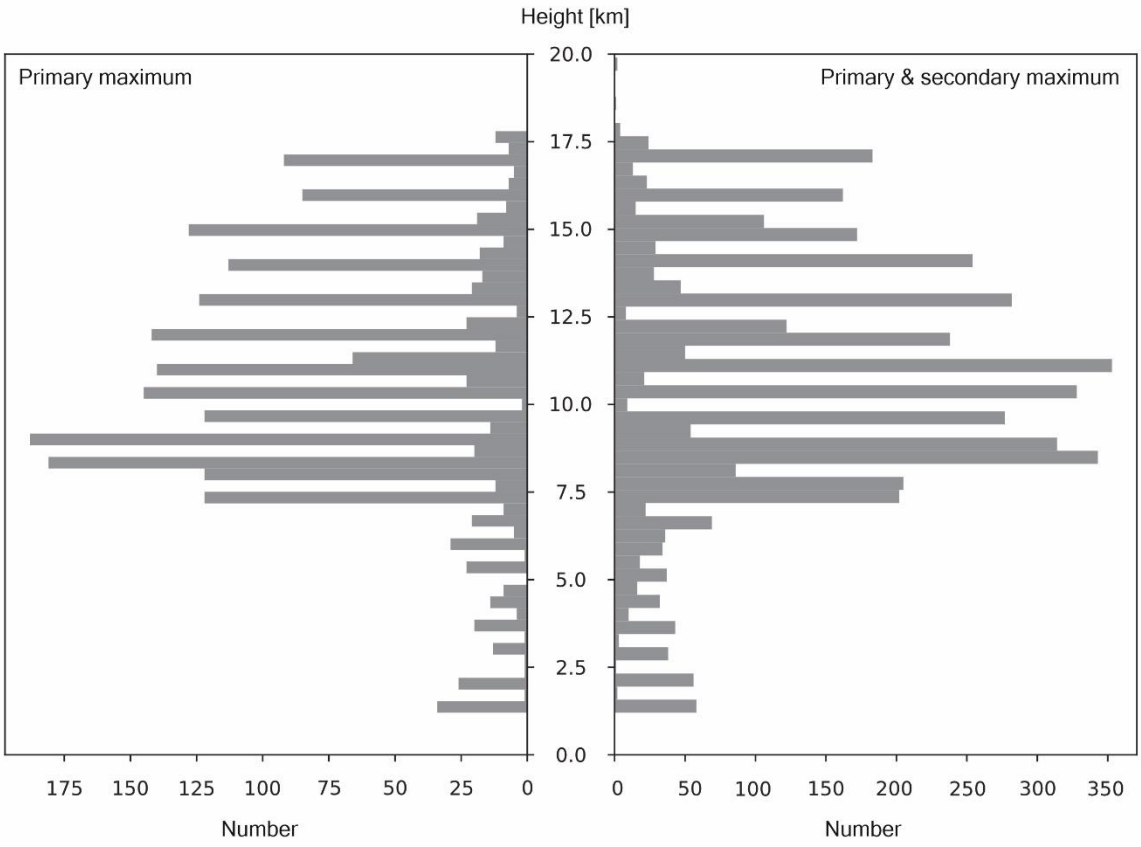

Figure 10 While the left part shows the height of the primary wind maximum of each vertical wind profile used for the derivation of E_{kin}, the right part includes also the secondary maximum.

7 Summary and outlook

The question which we addressed in this manuscript was whether enhanced values of GW kinetic energy density estimates over the Northern Atlantic and parts of Europe and Africa (25–70°N and 45°W–20°E) can be observed during the passage of two streamers, one in February and the other one in November 2020, based on Aeolus data after the streamers have been identified in auxiliary data (total column ozone measurements).

Streamers, which are linked to several possible GW sources such as a pressure system, frontal activity and wind shear, are due to enhanced planetary waves. They can be identified very well in TO3 maps from GOMOS or TROPOMI, for example. To the best of our knowledge, they have not been analysed in the context of GW sources.

Aeolus measurements allow the derivation of E_{kin} in the altitude regions where streamers are present. However, this is challenging, as the GW-induced wind variations, which we derived by applying a repeating spline, lie in the same order of magnitude as the error of Aeolus. We tried to handle this challenge statistically by covering a large area and collecting around 100 profiles per day. Comparison of this daily averaged E_{kin} with the literature show that those values are at the upper border. This can be the result of a low precision of the Aeolus measurements, emphasises the need for validation campaigns to take place at the same time and in the same place and underlines the importance of specifying the systematic and the random part of an error.

In both streamer cases, we found significant local maxima in the daily resolved time series of E_{kin} in the lower stratosphere when the streamer passed the addressed geographical region. We also did a spatial analysis with a relative coarse spatial resolution of 7.5° in latitude and 10° in longitude (roughly 800 km in each direction for the mid-point of the addressed area). In order to get a reasonable amount of data per pixel, we applied a temporal resolution of one week. However, this resolution is not good enough to get more precise information about the region of enhanced E_{kin} and therefore about the possible GW generation mechanism.

In this manuscript, we focused only on the kinetic energy, however, GW transport not only kinetic energy, they also carry potential energy. For low-frequency waves, the relation of the horizontal kinetic energy densities and the potential energy density, $E_{kin,h}$ and E_{pot}, is determined by

$$\frac{\overline{E_{kin,h}}}{\overline{E_{pot}}} = \frac{1 + \left(\frac{f}{\widehat{\omega}}\right)^2}{1 - \left(\frac{f}{\widehat{\omega}}\right)^2} \tag{4}$$

(Geller and Gong, 2010). In their appendix B, Geller and Gong (2010) provide the above mentioned relation using the full GW dispersion relation. The authors state that the asymptotic behaviour of the equation above based on the full dispersion relation and the dispersion relation for low-frequency waves is similar. Since a succeeding mission for Aeolus is planned, which reaches also higher altitudes, information about $E_{kin,h}$ might be available even higher up in future. For the calculation of E_{pot}, vertical

temperature profiles are needed. Those are currently available through TIMED-SABER or GPS radio occultation satellites, for example. Given that the wind and the temperature measurements address approximately the same air volume at the same time, which is not the case for TIMED-SABER and Aeolus in the vast majority of cases, $\hat{\omega}$ can be estimated. $\hat{\omega}$ is an important parameter for calculating further GW information such as ratio of the vertical to the horizontal group velocity for low-frequency waves or the angle between lines of constant phase and the vertical for high-frequency waves, etc. In conclusion, it would be helpful for GW analyses, if Aeolus is synchronized with a temperature mission.

Author contribution

This work was funded by two projects: LISA and WAVE. The first one was acquired by LK, SW and MB, the second one by SW and MB. The streamer events were identified by FT and LK and checked by SW. The GW analyses were performed by SW. The manuscript was written by SW. All authors read the manuscript.

Acknowledgement

The work of Sabine Wüst was funded by the European Space Agency, ESA, (project LISA, ESA Contract No. 4000133567/20/I-BG) and the Bavarian State Ministry for the Environment and Consumer Protection (WAVE, TKO01KPB-73893). The work of Lisa Küchelbacher was funded in parts by the European Space Agency, ESA, (project LISA).
We thank Oleg Goussev and Isabell Krisch (both DLR) for their support concerning the Aeolus data download.
Finally, we would like to thank the anonymous reviewers for the valuable comments.

Code / Data availability

The detrending algorithm is described in Wüst et a. (2017). The Aeolus data was downloaded from the ESA Aeolus Online Dissemination System (https://aeolus-ds.eo.esa.int/oads/access/, last download: 1st Dec. 2020).

Competing interest

The authors declare that they have no conflict of interest.

References

Alexander, M. J., Geller, M., McLandress, C., Polavarapu, S., Preusse, P., Sassi, F., Eckermann, S., Ern, M., Hertzog, A., Kawatani, Y., Pulido, M., Shaw, T. A., Sigmond, M., Vincent, R. and Watanabe, S.: Recent developments in gravity-wave effects in climate models and the global distribution of gravity-wave momentum flux from observations and models. Quarterly Journal of the Royal Meteorological Society, 136(650), 1103-1124, https://doi.org/10.1002/qj.637, 2010.

Banyard, T. P., Wright, C. J., Hindley, N. P., Halloran, G., Krisch, I., Kaifler, B., and Hoffmann, L.: Atmospheric gravity waves in Aeolus wind lidar observations, Geophysical Research Letters, 48, e2021GL092756, https://doi.org/10.1029/2021GL092756, 2021.

Nath, D., Venkat Ratnam, M., Jagannadha Rao, V. V. M., Krishna Murthy, B. V., and Vijaya Bhaskara Rao, S.: Gravity wave characteristics observed over a tropical station using high-resolution GPS radiosonde soundings, Journal of Geophysical Research, 114, D06117, doi:10.1029/2008JD011056, 2009.

Dhadly, M. S., Englert, C. R., Drob, D. P., Emmert, J. T., Niciejewski, R., and Zawdie, K. A.: Comparison of ICON/MIGHTI and TIMED/TIDI neutral wind measurements in the lower thermosphere, Journal of Geophysical Research: Space Physics, 126, e2021JA029904, https://doi.org/10.1029/2021JA029904, 2021.

Dutta, G., Vinay Kumar, P., and Mohammad, S.: Retrieving characteristics of inertia gravity wave parameters with least uncertainties using the hodograph method, Atmospheric Chemistry and Physics, 17, 14811–14819, https://doi.org/10.5194/acp-17-14811-2017, 2017.

Eichinger, R., Garny, H., Šácha, P., Danker, J., Dietmüller, S., and Oberländer-Hayn, S.: Effects of missing gravity waves on stratospheric dynamics; part 1: climatology. Climate Dynamics, 54, 3165-3183, https://doi.org/10.1007/s00382-020-05166-w, 2020.

Englert, C. R., Harlander, J. M., Brown, C. M., Marr, K. D., Miller, I. J., Stump, J. E., Hancock, J., Peterson, J. Q., Kumler, J., Morrow, W. H., Mooney, T. A., Ellis, S., Mende, S. B., Harris, S. E., Stevens, M. H., Makela, J. J., Harding, B. J., and Immel, T. J.: Michelson Interferometer for Global High-Resolution Thermospheric Imaging (MIGHTI): Instrument Design and Calibration, Space Science Reviews, 212, 553–584, https://doi.org/10.1007/s11214-017-0358-4, 2017.

Ern, M., Trinh, Q. T., Preusse, P., Gille, J. C., Mlynczak, M. G., Russell III, J. M., and Riese, M.: GRACILE: a comprehensive climatology of atmospheric gravity wave parameters based on satellite limb soundings, Earth System Science Data, 857–892, https://doi.org/10.5194/essd-10-857-2018, 2018.

Forbes, J. M.: Tidal and planetary waves, The upper mesosphere and lower thermosphere: A review of experiment and theory, 87, 67 – 87, 1995.

Fritts, D. C. and Alexander, M. J.: Gravity wave dynamics and effects in the middle atmosphere, Reviews of Geophysics, 41, https://doi.org/10.1029/2001RG000106, 2003.

Fritts, D. C. and Nastrom, G. D.: Sources of Mesoscale Variability of Gravity Waves. Part II: Frontal, Convective, and Jet Stream Excitation, Journal of Atmospheric Sciences, 49, 111–127, https://doi.org/10.1175/1520-0469(1992)049<0111:SOMVOG>2.0.CO;2, available at: https://journals.ametsoc.org/view/journals/atsc/49/2/1520-0469_1992_049_0111_somvog_2_0_co_2.xml, 1992.

Geller, M. A. and Gong, J.: Gravity wave kinetic, potential, and vertical fluctuation energies as indicators of different frequency gravity waves, Journal of Geophysical Research: Atmospheres, 115, https://doi.org/10.1029/2009JD012266, 2010.

Hocke, K., Schranz, F., Maillard Barras, E., Moreira, L., and Kämpfer, N.: An Atlantic streamer in stratospheric ozone observations and SD-WACCM simulation data, Atmospheric Chemistry and Physics, 17, 3445–3452, https://doi.org/10.5194/acp-17-3445-2017, 2017.

Holton, J. R.: The role of gravity wave induced drag and diffusion in the momentum budget of the mesosphere, J. Atmos. Sci., 39, 791–799, 1982.

Houghton, J.: The Physics of Atmospheres, Cambridge University Press, 2002.

Khaykin, M. S., Hauchecorne, A., Wing, R., Keckhut, P., Godin-Beekmann, S., Porteneuve, J., Mariscal, J.-F., and Schmitt, J.: Doppler lidar at Observatoire de Haute-Provence for wind profiling up to 75 km altitude: Performance evaluation and observations, Atmospheric Measurement Techniques, 13, 1501–1516, https://doi.org/10.5194/amt-13-1501-2020, available at: https://www.scopus.com/inward/record.uri?eid=2-s2.0-85082922216&doi=10.5194%2famt-13-1501-2020&partnerID=40&md5=6d36307b057608af731a847968ccbfce, 2020.

Kramer, R., Wüst, S., and Bittner, M.: Investigation of gravity wave activity based on operational radiosonde data from 13 years (1997-2009): Climatology and possible induced variability, Journal of Atmospheric and Solar-Terrestrial Physics, 140, 23–33, https://doi.org/10.1016/j.jastp.2016.01.014, 2016.

Kramer, R., Wüst, S., Schmidt, C., and Bittner, M.: Gravity wave characteristics in the middle atmosphere during the CESAR campaign at Palma de Mallorca in 2011/2012: Impact of extratropical cyclones and cold fronts, Journal of Atmospheric and Solar-Terrestrial Physics, 128, 8–23, https://doi.org/10.1016/j.jastp.2015.03.001, 2015.

Krisch, I., Hindley, N. P., Reitebuch, O., and Wright, C. J.: On the derivation of zonal and meridional wind components from Aeolus horizontal line-of-sight wind, Atmos. Meas. Tech., 15, 3465–3479, https://doi.org/10.5194/amt-15-3465-2022, 2022.

Krüger, K., Langematz, U., Grenfell, J. L., and Labitzke, K.: Climatological features of stratospheric streamers in the FUB-CMAM with increased horizontal resolution, Atmospheric Chemistry and Physics, 5, 547–562, https://doi.org/10.5194/acp-5-547-2005, 2005.

Loyola, D. G., Koukouli, M. E., Valks, P., Balis, D. S., Hao, N., Van Roozendael, M., Spurr, R. J. D., Zimmer, W., Kiemle, S. Lerot, C. and Lambert, J. C.: The GOME-2 total column ozone product: Retrieval algorithm and ground-based validation. Journal of Geophysical Research: Atmospheres, 116(D7), https://doi.org/10.1029/2010JD014675, 2011.

Martin, A., Weissmann, M., Reitebuch, O., Rennie, M., Geiß, A., and Cress, A.: Validation of Aeolus winds using radiosonde observations and numerical weather prediction model equivalents, Atmospheric Measurement Techniques, 14, 2167–2183, https://doi.org/10.5194/amt-14-2167-2021, 2021.

McIntyre, M. E., and Palmer, T. N.: Breaking planetary waves in the stratosphere. Nature, 305(5935), 593–600, https://doi.org/10.1038/305593a0 , 1983.

Moffat-Griffin, T., Wright, C. J., Moss, A. C., King, J. C., Colwell, S. R., Hughes, J. K., and Mitchell, N. J.: The South Georgia Wave Experiment (SG-WEX): Radiosonde observations of gravity waves in the lower stratosphere. Part I: Energy density, momentum flux and wave propagation direction. Quarterly Journal of the Royal Meteorological Society, 143(709), 3279 – 3290, https://doi.org/10.1002/qj.31812017.

Munro, R., Eisinger, M., Anderson, C., Callies, J., Corpaccioli, E., Lang, R., Lefebvre, A., Livschitz, Y. and Albinana, A. P.: GOME-2 on MetOp. In Proc. of The 2006 EUMETSAT Meteorological Satellite Conference, Helsinki, Finland (Vol. 1216, p. 48), 2006.

Munro, R., Lang, R., Klaes, D., Poli, G., Retscher, C., Lindstrot, R., Huckle, R., Lacan, A., Grzegorski, M., Holdak, A., Kokhanovsky, A., Livschitz, J., and Eisinger, M.: The GOME-2 instrument on the Metop series of satellites: instrument design, calibration, and level 1 data processing – an overview, Atmospheric Measurement Techniques, 9, 1279–1301, https://doi.org/10.5194/amt-9-1279-2016, 2016.

Murphy, D. J., Alexander, S. P., Klekociuk, A. R., Love, P. T., and Vincent, R. A.: Radiosonde observations of gravity waves in the lower stratosphere over Davis, Antarctica, Journal of Geophysical Research Atmosphere, 119, 11,973–11,996, https://doi.org/10.1002/2014JD022448, 2014.

Nappo, C. J.: An Introduction to Atmospheric Gravity Waves, 2nd ed., Elsevier Science, Netherlands, 2013.

Niciejewski, R., Wu, Q., Skinner, W., Gell, D., Cooper, M., Marshall, A., Killeen, T., Solomon, S., and Ortland, D.: TIMED Doppler Interferometer on the Thermosphere Ionosphere Mesosphere Energetics and Dynamics satellite: Data product overview, Journal of Geophysical Research: Space Physics, 111, https://doi.org/10.1029/2005JA011513, 2006.

Offermann, D., Grossmann, K.-U., Barthol, P., Knieling, P., Riese, M., and Trant, R.: Cryogenic Infrared Spectrometers and Telescopes for the Atmosphere (CRISTA) experiment and middle atmosphere variability, Journal of Geophysical Research: Atmospheres, 104, 16311–16325, https://doi.org/10.1029/1998JD100047, 1999.

675 Plougonven, R. and Zhang, F.: Internal gravity waves from atmospheric jets and fronts, Reviews of Geophysics, 52, 33–76, https://doi.org/10.1002/2012RG000419, 2014.

Polvani, L. M., and Plumb, R. A.: Rossby wave breaking, microbreaking, filamentation, and secondary vortex formation: The dynamics of a perturbed vortex. Journal of Atmospheric Sciences, 49(6), 462-476, https://doi.org/10.1175/1520-0469(1992)049<0462:RWBMFA>2.0.CO;2, 1992.

680 Pramitha, M., Venkat Ratnam, M., Taori, A., Krishna Murthy, B. V., Pallamraju, D., and Vijaya Bhaskar Rao, S.: Evidence for tropospheric wind shear excitation of high-phase-speed gravity waves reaching the mesosphere using the ray-tracing technique. Atmospheric Chemistry and Physics, 15(5), 2709-2721, https://doi.org/10.5194/acp-15-2709-2015, 2015.

Preusse, P., Dörnbrack, A., Eckermann, S. D., Riese, M., Schaeler, B., Bacmeister, J. T., Broutman, D., and Grossmann, K. U.: Space-based measurements of stratospheric mountain waves by CRISTA 1. Sensitivity, analysis method, and a case
685 study. Journal of Geophysical Research: Atmospheres, 107(D23), CRI-6, https://doi.org/10.1029/2001JD000699, 2002.

Ratynski, M., Khaykin, S., Hauchecorne, A., Wing, R., Cammas, J.-P., Hello, Y., and Keckhut, P.: Validation of Aeolus wind profiles using ground-based lidar and radiosonde observations at Réunion island and the Observatoire de Haute-Provence, Atmospheric Measurement Techniques, 997–1016, https://doi.org/10.5194/amt-16-997-2023, 2023.

Rauthe, M., Gerding, M., and Lübken, F.-J.: Seasonal changes in gravity wave activity measured by lidars at mid-latitudes,
690 Journal of Atmospheric Chemistry and Physics, 13741–13773, https://doi.org/10.5194/acp-8-6775-2008, 2008.

Reitebuch, O., Lemmerz, C., Lux, O., Marksteiner, U., Rahm, S., Weiler, F., Witschas, B., Meringer, M., Schmidt, K., Huber, D., Nikolaus, I., Geiss, A., Vaughan, M., Dabas, A., Flament, T., Stieglitz, H., Isaksen, L., Rennie, M., Kloe, J. D., Marseille, G.-J., Stoffelen, A., Wernham, D., Kanitz, T., Straume, A.-G., Fehr, T., Bismarck, J. von, Floberghagen, R., and Parrinello, T.: Initial Assessment of the Performance of the First Wind Lidar in Space on Aeolus, EPJ Web Conf, 237,
695 1010, https://doi.org/10.1051/epjconf/202023701010, 2020.

Rennie, M.P., Isaksen, L., Weiler, F., de Kloe, J., Kanitz, T. & Reitebuch, O.: The impact of Aeolus wind retrievals on ECMWF global weather forecasts. Quarterly Journal of the Royal Meteorological Society, 147, 3555–3586. https://doi.org/10.1002/qj.4142, 2021.

- Rennie, M.P., Isaksen, L.: The NWP impact of Aeolus Level-2B winds at ECMWF, ESA Contract Report, 02/2024.
700 https://www.ecmwf.int/en/elibrary/81546-nwp-impact-aeolus-level-2b-winds-ecmwf, last access, 7th Nov. 2024, 2024.

Spurr R., Loyola D., Heue K.-P., v. Roozendael M., Lerot C.: S5P/TROPOMI Total Ozone ATBD. No. S5P-L2-DLR-ATBD-400A, 2022.

Tan, D. G. H., Andersson, E., Kloe, J. D., Marseille, G.-J., Stoffelen, A., Poli, P., Denneulin, M.-L., Dabas, A., Huber, D., Reitebuch, O., Flamant, P., Le Rille, O., and Nett, H.: The Aeolus wind retrieval algorithms, Tellus A: Dynamic Meteorology and Oceanography, 60, 191–205, https://doi.org/10.1111/j.1600-0870.2007.00285.x, 2008.

Veefkind, J.P., Aben, I., McMullan, K., Förster, H., de Vries, J., Otter, G., Claas, J., Eskes, H.J., de Haan, J.F., Kleipool, Q., van Weele, M., Hasekamp, O., Hoogeveen, R., Landgraf, J., Snel, R., Tol, P., Ingmann, P., Voors, R., Kruizinga, B., Vink, R., Visser, H. and Levelt, P.F.: TROPOMI on the ESA Sentinel-5 Precursor: A GMES mission for global observations of the atmospheric composition for climate, air quality and ozone layer applications. Remote sensing of environment, 120, 70-83, https://doi.org/10.1016/j.rse.2011.09.027, 2012.

Witschas, B., Lemmerz, C., Geiß, A., Lux, O., Marksteiner, U., Rahm, S., Reitebuch, O., Schäfler, A., and Weiler, F.: Validation of the Aeolus L2B wind product with airborne wind lidar measurements in the polar North Atlantic region and in the tropics, Atmospheric Measurement Techniques, 15, 7049–7070, https://doi.org/10.5194/amt-15-7049-2022, available at: https://amt.copernicus.org/articles/15/7049/2022/, 2022.

Wüst, S., Wendt, V., Linz, R., and Bittner, M.: Smoothing data series by means of cubic splines: quality of approximation and introduction of a repeating spline approach, Atmospheric Measurement Techniques, 10, 3453–3462, https://doi.org/10.5194/amt-10-3453-2017, 2017.

Wüst, S., Wendt, V., Schmidt, C., Lichtenstern, S., Bittner, M., Yee, J.-H., Mlynczak, M. G., and Russell III, J. M.: Derivation of gravity wave potential energy density from NDMC measurements, Journal of Atmospheric and Solar-Terrestrial Physics, 138, 32–46, https://doi.org/10.1016/j.jastp.2015.12.003, 2016.

Yoshiki, M., and Sato, K. A statistical study of gravity waves in the polar regions based on operational radiosonde data. Journal of Geophysical Research: Atmospheres, 105, D14, 17995-18011, 2000.

Zülicke, C. and Peters, D.: Parameterization of strong stratospheric inertia–gravity waves forced by poleward-breaking Rossby waves, Monthly weather review, 136, 98–119, https://doi.org/10.1175/2007MWR2060.1, 2008.